Journal of
Materials Chemistry A

A Simple Chemical Guide for Finding Novel n-type Dopable Zintl Pnictide Thermoelectric Materials

Journal:	*Journal of Materials Chemistry A*
Manuscript ID	TA-ART-04-2019-003786.R1
Article Type:	Paper
Date Submitted by the Author:	12-Jul-2019
Complete List of Authors:	Gorai, Prashun; Colorado School of Mines Goyal, Anuj; Colorado School of Mines Toberer, Eric; Colorado School of Mines, Stevanovic, Vladan; Colorado School of Mines

SCHOLARONE™
Manuscripts

Journal Name

A Simple Chemical Guide for Finding Novel *n*-type Dopable Zintl Pnictide Thermoelectric Materials[†]

Prashun Gorai,[*a] Anuj Goyal,[a] Eric S. Toberer,[b] and Vladan Stevanović[*a]

Computations have predicted good thermoelectric performance for a number of Zintl phases when doped *n*-type. Combined with the successful experimental realization of *n*-type $KGaSb_4$, $KAlSb_4$, and Mg_3Sb_2 with $zT \gtrsim 1$, this has fueled efforts to discover novel *n*-type dopable Zintl phases. However, a majority of Zintl phases exhibit strong proclivity toward *p*-type doping and prior successes in finding *n*-type dopable Zintls were largely serendipitous. Herein we use modern first-principles defect calculations to study trends in the dopability of Zintl pnictides and find that the average oxidation state of the anion is a useful chemical guide to identify novel *n*-type dopable phases. Specifically, we observe that Zintl pnictides with average oxidation of the anion near -1 are *n*-type dopable. The trend is mainly a consequence of the high formation energy of native acceptor defects (*e.g.* cation vacancies) and the resulting absence of charge (electron) compensation. Using the oxidation state guide in conjunction with a descriptor of thermoelectric performance, we conduct a large-scale materials search and identify promising candidates that are *n*-type dopable.

1 Introduction

Zintl phases are composed of electropositive cations (*e.g.* alkali, alkaline, rare-earths) that are ionically bonded to a polyanionic framework, typically consisting of covalent anion-anion bonds,[1] as shown for $KGaSb_4$ in Figure 1. Zintl phases continue to intrigue chemists because of their unique characteristics, including dispersive bands, small band gaps[2], and weakly bound cations[3]. Together, these yield materials with excellent charge transport and poor phonon transport. These attributes make Zintl phases particularly suitable for thermoelectric applications[4–13]. Indeed, they are among the best thermoelectric materials, with demonstrated thermoelectric figure of merit $zT > 1$ for *p*-type $Yb_{14}MnSb_{11}$[14], $Ca_9Zn_{4+x}Sb_9$[15], $Ca_{0.5}Yb_{0.5}Mg_2Bi_2$[16], and $Ba_8Ga_{16}Ge_{30}$[17]. While Zintl phases, in general, span a diverse range of chemistries, many Zintl thermoelectric materials are pnictides, *i.e.*, compounds containing group 15 anions such as As, Sb, and Bi. It is for this reason that we focus on Zintl pnictides in this study.

It is not surprising that Zintl pnictides exhibit good thermoelectric performance for *p*-type doping because the majority of them are, as grown, natively *p*-type due to self-doping. Examples of *p*-type Zintl pnictides include the "14-1-11" phases[18] (*e.g.* $Yb_{14}MgBi_{11}$), "1-2-2" phases[19] (*e.g.* $SrZn_2Sb_2$), "5-2-6" phases[12] (*e.g.* $Ca_5Al_2Sb_6$), "16-11" phases[20] (*e.g.* $Ca_{16}Bi_{11}$) etc. Hence,
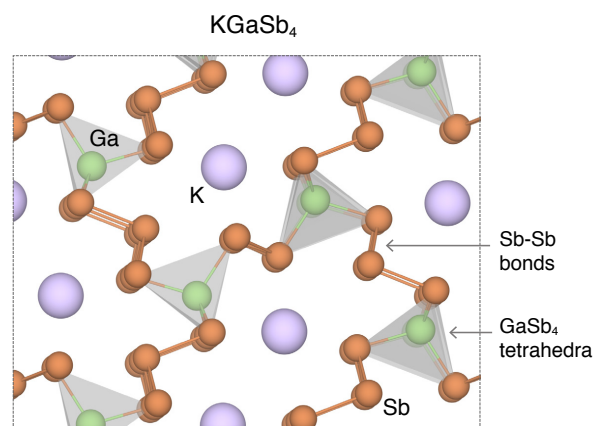
Fig. 1 Crystal structure of a Zintl phase, $KGaSb_4$, with an anionic framework composed of $GaSb_4$ tetrahedra linked by Sb-Sb bonds and the interstices filled with electropositive K cations.

efforts to improve their thermoelectric performance have focused mainly on optimizing hole conductivity through extrinsic doping. Few attempts have been made to dope Zintl pnictides *n*-type; it is only recently that *n*-type doping has been experimentally demonstrated in a handful of Zintl phases. The most prominent example is *n*-type Mg_3Sb_2 with a maximal achieved zT in excess of 1.5[21–23], followed by *n*-type $KAlSb_4$[24] and $KGaSb_4$[25] with $zT \approx 1$, which was achieved without optimization of the transport properties. However, a recent study has shown that Mg_3Sb_2 is not a

*[a]Metallurgical and Materials Engineering, Colorado School of Mines, Golden, CO 80401. [b]Physics, Colorado School of Mines, Golden, CO 80401. *E-mail: pgorai@mines.edu, vstevano@mines.edu*

layered material and therefore, the Zintl-Klemm concept cannot be invoked to rationalize it as a Zintl phase.[26] The discovery of *n*-type dopable Zintl pnictides was largely serendipitous and driven mainly by chemical intuition. An accurate and quantitative understanding of the dopability Zintl pnictides is still lacking. Interestingly, the potential for good thermoelectric performance of Zintl pnictides, if doped *n*-type, was first suggested in computational searches[24,27] and subsequently, validated through experiments[24,25,27].

The observed strong proclivity of Zintl pnictides toward *p*-type conductivity is generally due to the facile formation of native acceptor defects, typically cation vacancies – they act as "killer" defects by charge compensating electrons from native and extrinsic donors. The facile formation of cation vacancies is plausibly a consequence of the weak chemical bonding of the cations to the anionic framework. Conversely, cation vacancies likely have high formation energies in *n*-type dopable Zintl pnictides,[23,25] which prevents electron compensation.

In this work, we use modern defect theory and first-principles defect calculations to investigate the dopability and the existence of design principles for *n*-type doping of Zintl pnictides. These design principles could be used in conjunction with descriptors of thermoelectric performance to advance the computational search for novel Zintl thermoelectric materials. We identify a simple, yet effective, chemical guide that correlates with the *n*-type dopability of Zintl pnictides. Specifically, we observe that Zintls with average oxidation state of the anion (pnictogen) near -1 are *n*-type dopable. This observation follows from the analysis of the chemical composition of *n*-type dopable Zintl pnictides, as determined from our defect calculations. Interestingly, we find that in Zintl pnictides with average pnictide oxidation state near -1, the formation of cation vacancies is suppressed, which makes them *n*-type dopable. The relatively high formation energy of the cation vacancies in these Zintl pnictides is likely due to their cation-poor chemical compositions such that formation of cation vacancies is energetically unfavorable. In contrast, known *p*-type dopable Zintl phases have cation-rich compositions, where cation vacancies form readily. We utilize our chemical guide in combination with a previously developed descriptor of thermoelectric performance[28] in a large-scale materials search and identify novel *n*-type dopable Zintl pnictides that are promising for thermoelectric applications. Furthermore, we confirm the *n*-type dopability of three candidate materials through direct defect calculations.

2 Results and Discussion

The dopability of a semiconductor, which is quantified as the achievable carrier type(s) and concentrations, depends on several factors, including the native defect energetics and the existence of dopants with sufficient solubility and desired electronic properties. Here, we focus on native defects under various growth conditions and how they allow or prevent the desired doping.

2.1 Role of Native Defects in Dopability

With the advent of first-principles computations, the formation energetics of point defects can be reliably calculated with stan-

dard methods such as the supercell approach[23,25,29]. The defect formation energy is calculated as:

$$\Delta H_{D,q} = (E_{D,q} - E_H) + qE_F + \sum_i n_i \mu_i + E_{corr} \tag{1}$$

where $E_{D,q}$ and E_H are the total energies of the supercell containing defect D in charge state q and the defect-free host supercell, respectively. E_F is the Fermi energy and E_{corr} comprises all the finite-size corrections that are applied within the supercell approach .[29] The dependence of the formation energy on the phase stability and growth conditions is captured by the term $\sum_i n_i \mu_i$. The chemical potential of element i is denoted by μ_i and n_i is the number of atoms of element i added ($n_i < 0$) or removed ($n_i > 0$) from the supercell. Conventionally, the elemental chemical potential μ_i is expressed relative to the reference elemental phase as $\mu_i = \mu_i^0 + \Delta\mu_i$, where μ_i^0 is the reference chemical potential under standard conditions and $\Delta\mu_i$ is the deviation from the reference chemical potential. $\Delta\mu_i = 0$ corresponds to *i*-rich growth conditions while large negative values of $\Delta\mu_i$ correspond to *i*-poor growth conditions. The bounds on $\Delta\mu_i$ for a given material are set by the region of phase stability. Further computational details are provided in the Methods section.

Computed defect energetics are typically presented in the form of a "defect diagram" – formation energies ($\Delta H_{D,q}$) of defects plotted as functions of Fermi energy (E_F) (see following sections for several examples). For each defect, the trace corresponding to the charge state with lowest $\Delta H_{D,q}$ at a given Fermi energy is drawn. The slope of the trace is the charge state of the defect because of the linear dependence in Eq. 1. Defects with positive and negative slopes are donors and acceptors, respectively, while those with zero slope are charge neutral. As described above, the defect energetics also depends on the growth conditions, which is quantified by the $\Delta\mu$ of each of the elements present in the compound. Therefore, a different "defect diagram" exists for each unique growth conditions.

Under a given growth condition, the equilibrium E_F and the corresponding free carrier concentration is determined by solving the condition of charge neutrality[30,31]. The concentration of donor and acceptor defects are determined using a Boltzmann distribution, such that $[D_q] = N_s e^{-\Delta H_{D,q}/k_B T}$, where $[D_q]$ is the defect concentration, N_s is the concentration of lattice sites where the defect can be formed, k_B is the Boltzmann constant, and T is the temperature. Here, $\Delta H_{D,q}$ is a function of E_F ("defect diagram"). The concentrations of electrons and holes at a given T are also functions of E_F. To establish charge neutrality, the total positive charges should equal the negative charges. In this equation, at a given temperature, the Fermi energy is the only free parameter. Solving the charge neutrality condition self-consitently yields the equilibrium E_F; the corresponding free carrier concentration can then be determined straightforwardly. In computing the carrier concentration, typically, the synthesis temperature is used because it is assumed that the defect concentrations at higher temperatures are "frozen-in" (quenched). A change in the defect concentrations require significant atomic rearrangement, which is likely to be kinetically limited at low temperatures.

The dopability of a material is often limited by their native de-
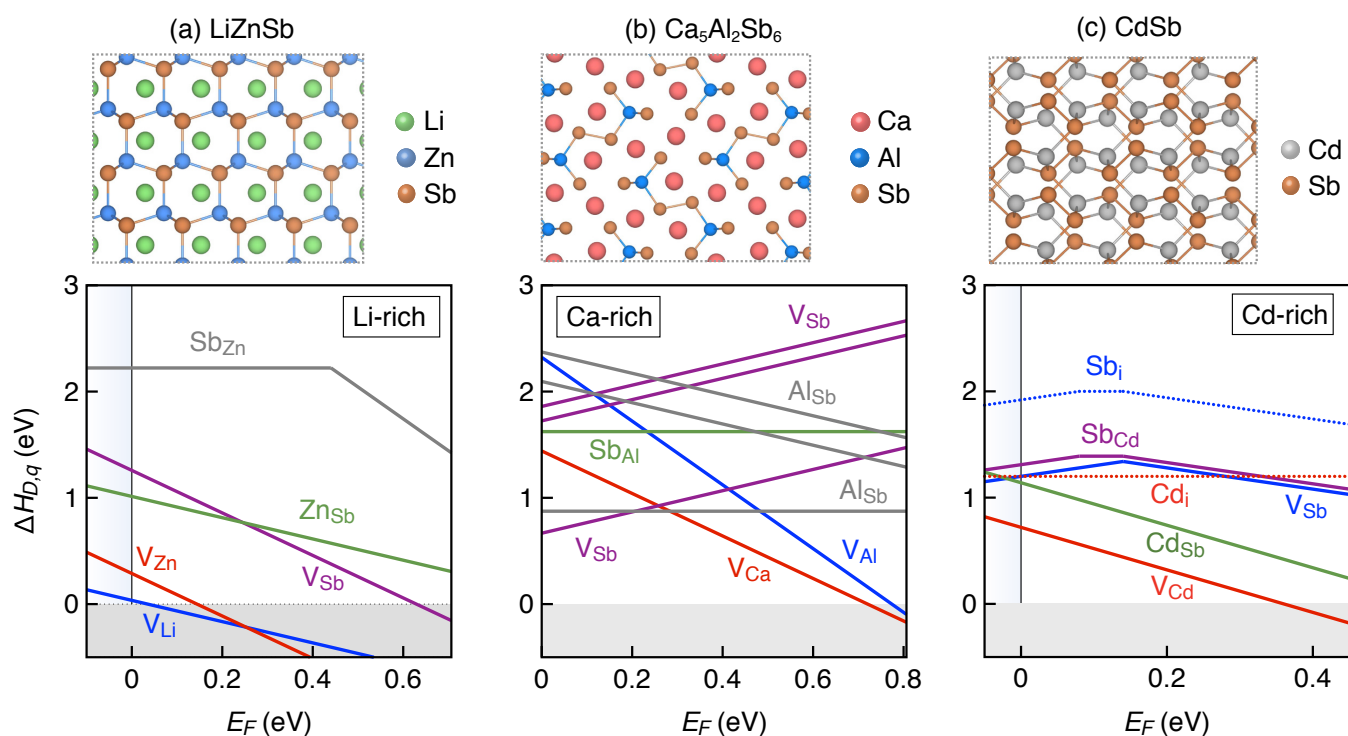
Fig. 2 Formation energies of native defects ($\Delta H_{D,q}$) as functions of Fermi energy (E_F) for (a) LiZnSb, (b) Ca$_5$Al$_2$Sb$_6$, and (c) CdSb under Li-rich, Ca-rich, and Cd-rich growth conditions, respectively. The corresponding crystal structures are shown above. E_F is referenced to the valence band maximum. The upper limit of E_F shown is the conduction band minimum such that E_F values range from 0 to the band gap. Multiple lines of the same color represent the same defect type at different Wyckoff sites. The shaded region on the left in (a) represents the valence band. $\Delta H_{D,q}$ of some defects, particularly interstitials, are outside the energy window shown. Low $\Delta H_{D,q}$ of "killer" cation vacancies hinder n-type doping.

fects. For instance, when acceptor defects with low formation energy (high concentration) are present, the material can be only doped p-type; in such cases, n-type doping may lead to low free electron concentration or it may not be possible altogether. Such acceptor defects are colloquially termed electron "killers" because they limit n-type doping.

2.2 Defect Chemistry of p-type Zintl Pnictides

Many well-known Zintl phases, such as Ca$_5$Al$_2$Sb$_6$ and CaZn$_2$Sb$_2$ are examples of materials where cation vacancies act as "killer" defects to limit n-type doping.[32] Conversely, the absence of acceptor defects with low formation energy presents an opportunity for n-type doping. Analogous arguments can be drawn for the role of native donor defects in p-type dopability. As discussed earlier, defect energetics and therefore, dopability, is a also a function of the growth conditions expressed in terms of the chemical potentials of the constituent elements. A material may also be both n- and p-type dopable under all growth conditions or n-type dopable under certain growth conditions while p-type under another growth condition. KGaSb$_4$, a recently discovered Zintl thermoelectric material[25], is an example of the former while PbTe and Mg$_3$Sb$_2$ are examples of the latter[22,23,31]. More specifically, Mg$_3$Sb$_2$ is doped p-type when grown under Mg-poor conditions[33] and n-type under Mg-rich conditions.[23]

The pervasiveness of electron "killer" defects in Zintl pnictides

has been extensively documented and characterized through both experiments[1,19,32] and theory[34]. A Zintl pnictide that is notorious for being degenerately p-type under all growth conditions is LiZnSb[35]. In 2006, Madsen performed one of the first high-throughput computational searches[36] for identifying thermoelectric materials – LiZnSb emerged as a promising n-type candidate. However, the computational search, like other computational searches that followed[28,37,38], was agnostic of material dopability. Subsequent experimental efforts to dope LiZnSb n-type were futile[35]; even lowering the hole concentration to below 10^{20} cm^{-3} proved daunting. In the absence of detailed defect characterization or calculated formation energetics, it was speculated that facile formation of one of the cation vacancies (V$_{Li}$ or V$_{Zn}$) resulted in degenerate hole doping.

To quantitatively understand the role of native defects in the p-type behavior of LiZnSb, we performed first-principles calculations – the computed defect energetics are presented in the form of a "defect diagram" in Figure 2(a). It is evident that acceptor Li vacancies (V$_{Li}$) have low formation energy even at the most Li-rich conditions allowed by the phase stability (equilibrium with Li$_3$Sb with $\Delta\mu_{Li}$ = -0.98 eV). The formation energy of V$_{Li}$ is noticeably small such that the equilibrium Fermi energy at 873 K lies inside the valence band and the free hole concentrations are in the degenerate limit (6×10^{20} cm^{-3}). The corresponding V$_{Li}$ concentration is ~4% of the Li site concentration, which is consistent with the observed significant off-stoichiometry in LiZnSb[35]. The
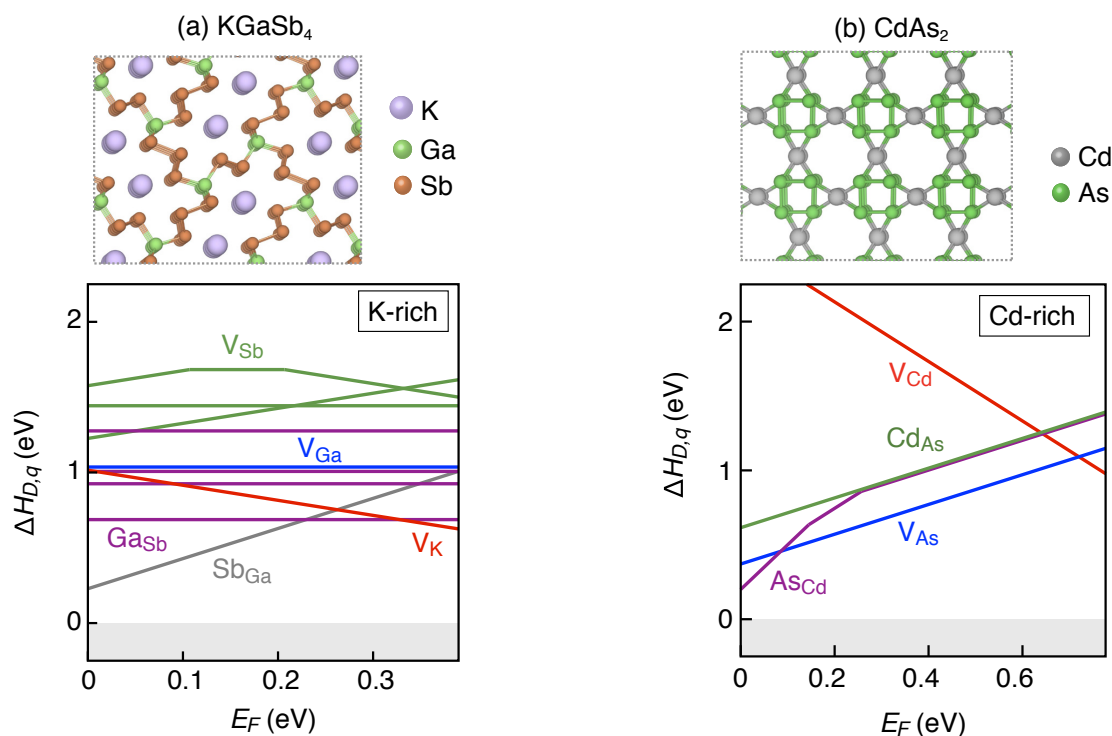
Fig. 3 Formation energies of native defects ($\Delta H_{D,q}$) as functions of Fermi energy (E_F) for (a) KGaSb$_4$, and (b) CdAs$_2$ under K-rich, and Cd-rich growth conditions, respectively. The corresponding crystal structures are shown above. E_F is referenced to the valence band maximum. The upper limit of E_F shown is the conduction band minimum such that E_F values range from 0 to the band gap. Multiple lines of the same color represent the same defect type at different Wyckoff sites. $\Delta H_{D,q}$ of some defects, particularly interstitials, are outside the energy window shown. In these materials, the formation energies of cation vacancies are relatively higher compared to the Zintl phases in Figure 2, which facilitates extrinsic n-type doping.

defect energetics presented in Figure 2(a) correspond to growth under relatively Li-rich conditions – this is intentional because the formation energy of V_{Li} is highest under the most Li-rich conditions and provides the lower bound for the hole concentration. From another perspective, the Li-rich conditions offer the best scenario to guage opportunities for n-type doping of LiZnSb. Given the facile formation of the "killer" defect V_{Li}, it is not possible to n-type dope LiZnSb, at least under equilibrium growth conditions.

To further our understanding of defect-limited dopability of Zintl pnictide phases, we consider the well-known Ca$_5$M$_2$Sb$_6$ family (M = Al, Ga, In) of p-type thermoelectric materials. The structure contains 1-D chains of corner-sharing MSb$_4$ tetrahedra that are linked by Sb-Sb bonds and interspered with Ca cations. Specifically, we calculated the native defect energetics of Ca$_5$Al$_2$Sb$_6$. Under both Ca-rich (Figure 2b) and Ca-poor conditions, we find that the acceptor-type Ca vacancies (V_{Ca}) are the lowest-energy defects and Ca$_5$Al$_2$Sb$_6$ is natively p-type, consistent with experiments[12]. The high formation energy of the lowest-energy donor V_{Sb} should facilitate extrinsic p-type doping. Indeed, Ca$_5$Al$_2$Sb$_6$ is known to be degenerately p-type doped with Na[12]. Additionally, it is known from experiments that M-site substitutions do not noticeably influence the hole concentrations[12], which further corroborates that Al vacancies, in fact, are not the predominant defects. As in the case of LiZnSb, the "killer" cation vacancies limit n-type doping of Ca$_5$Al$_2$Sb$_6$. However, the formation energy of Ca vacancies at Ca-rich conditions is not as low as

Li vacancies in LiZnSb.

Finally, we examine the native defect chemistry of CdSb, the lesser-known cousin of ZnSb – a material that has been widely investigated for thermoelectrics. CdSb possess the same orthorhombic structure as ZnSb and features the characteristic Sb-Sb covalent bonds (Figure 2c). As in the previous two examples, the cation vacancies (V_{Cd}) are the lowest-energy defects (Figure 2c) such that CdSb is natively p-type under Cd-rich as well as Cd-poor growth conditions. The defect chemistry of CdSb is similar to that of ZnSb, where the presence of large concentrations of Zn vacancies lead to degenerate hole doping.[34] In summary, the doping asymmetry of many Zintl pnictides that are only p-type doped (Figure 4) is attributed to the low formation energy of cation vacancies that act as electron "killers" and hinder n-type doping.

2.3 Defect Chemistry of Known n-type Dopable Zintls

Given the general scarcity of n-type Zintls, not much is known about their defect chemistry. Also, how the defect chemistry of n-type dopable Zintls differ from the persistently p-type Zintls (Section 2.2) remains to be understood. In this section, we present the computed defect energetics of two Zintl pnictides that are known to be n-type dopable: (1) KGaSb$_4$, which has been experimentally confirmed to be extrinsically dopable n-type with Ba[25], and (2) CdAs$_2$, an n-type Zintl with low electron concentrations in self-doped samples[39]. The calculated defect diagrams along with the

crystal structures are shown in Figure 3.

KGaSb$_4$ possess a tunnel-like structure formed by the anionic framework of GaSb$_4$ tetrahedra that are linked by Sb-Sb bonds (Figure 3a). The cation (K) occupies the large interstitial voids created by the tunnel structure. We have previously demonstrated through theory and experiments that n-type KGaSb$_4$ can be realized via Ba doping [25] resulting in electron concentrations of $\sim 10^{19}$ cm^{-3}. At first glance, the defect energetics of KGaSb$_4$ (Figure 3a) has one striking difference compared to the p-type Zintls discussed in Section 2.2 – the formation energy of all the defects is significantly higher in KGaSb$_4$, which has important implications for dopability. The lowest energy acceptor, as in p-type Zintl pnictides, is the cation vacancy (V$_K$). However, the formation energy of acceptor V$_K$ is fairly high such that their concentrations will be low, which will not hinder extrinsic n-type doping. The formation energy of V$_K$ is the highest under K-rich conditions (Figure 3a) offering the best opportunity to extrinsically n-type dope KGaSb$_4$. Another interesting observation from Figure 3(a) is that the lowest-energy native donor, the antisite Sb$_{Ga}$, also has a relatively high formation energy. This implies KGaSb$_4$ should also allow extrinsic p-type doping. Indeed, we have previously confirmed that KGaSb$_4$ is p-type doped with Zn [25], albeit the hole concentrations are lower than electron concentrations in n-type samples, consistent with the differences in formation energy of V$_K$ and Sb$_{Ga}$ at the CBM and VBM, respectively.. The lower hole concentrations in p-type samples can be attributed to the lower formation energy of Sb$_{Ga}$ compared to V$_K$ – some hole compensation by donor Sb$_{Ga}$ likely occurs when doped with Zn. Therefore, the defect calculations reveal that n-type doping of KGaSb$_4$ is enabled by the high formation energy of the otherwise "killer" acceptor cation vacancies.

Figure 3(b) shows the formation energies of the native defects in the binary Zintl phase, CdAs$_2$, under assumed Cd-rich growth conditions. The defect chemistry of CdAs$_2$ is qualitatively similar to KGaSb$_4$ in that the cation vacancies (V$_{Cd}$) have relatively high formation energies. In fact, the formation energy of V$_{Cd}$ at the conduction band minimum (CBM) is even higher than that of V$_K$ in KGaSb$_4$. As a result, extrinsic n-type doping of CdAs$_2$ grown under metal-rich conditions is very promising. Under Cd-rich conditions (Figure 3b), CdAs$_2$ is predicted to be natively n-type with low free electron concentration of 2×10^{17} cm^{-3} (T = 873 K). Available experimental reports confirm that self-doped CdAs$_2$ is indeed an n-type material with $\sim 10^{17}$ cm^{-3} free electron concentration [39]. It is also possible to realize p-type CdAs$_2$ via extrinsic doping because the formation energies of compensating donors, V$_{As}$ and antisite As$_{Cd}$ at the valence band maximum (VBM) under Cd-poor growth conditions are also relatively high.

In summary, we find that (1) the cation vacancies are one of the lowest-energy native acceptor defects, (2) the formation energies of cation vacancies are high, and (2) the Zintl phases may also be p-type dopable, making them good candidate materials for fabricating *both* n- and p-type legs of a thermoelectric device. Interestingly, we observe that the chemical compositions of KGaSb$_4$ and CdAs$_2$ are cation-poor; in contrast, the chemical compositions of known p-type Zintl pnictides are generally cation-rich (*e.g.* Ca$_5$Al$_2$Sb$_6$). As a consequence, we find that the
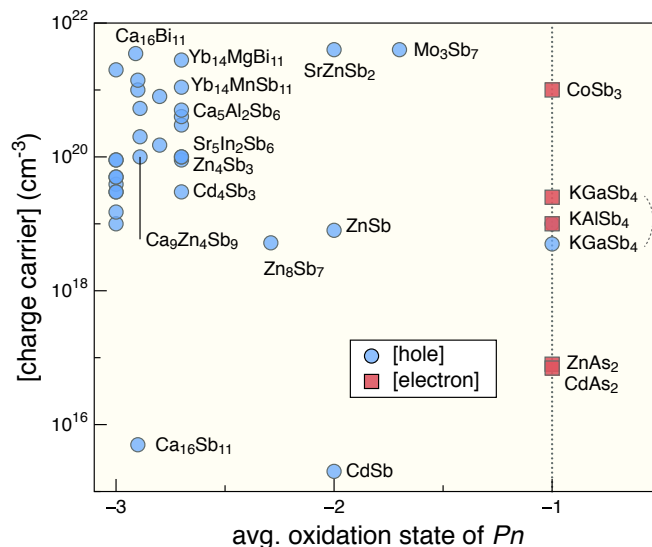
Fig. 4 Measured charge carrier concentrations of 40 known Zintl pnictides is shown as a function of the average oxidation state of the pnictide (*Pn*) anion. Blue circles denote p-type, red squares n-type. [12–15,18,20,22,23,32,39–64] KGaSb$_4$ can be doped both n- and p-type.

average oxidation state of the pnictide (Sb, As) is -1 in KGaSb$_4$ and CdAs$_2$, which are both n-type dopable. In comparison, the average pnictide oxidation state in known p-type Zintl phases is further from -1. For instance, -3 and -2 in LiZnSb and CdSb, respectively. To further build upon this observed correlation between n-type dopability and average pnictide oxidation state, we surveyed the experimental literature of Zintl pnictides, which is discussed next.

2.4 A Guide to Discover n-type Dopable Zintl Pnictides

Figure 4 presents the experimentally measured charge carrier (electrons, holes) concentrations of 40 Zintl pnictides as a function of the average oxidation state of the pnictide (*Pn*) anion. The average oxidation state of *Pn* is calculated by assuming the formal oxidation state of the cations and dividing the total positive valence with the number of *Pn* atoms. For example, in Ca$_9$Zn$_4$Sb$_9$, the formal oxidation states of Ca and Zn are 2+, such that the total positive valence is $9 \times 2 + 4 \times 2 = 26$, and therefore, average oxidation state of *Pn* is -26/9 = -2.89. Similarly, in KGaSb$_4$, the average oxidation state of *Pn* is $-(1+3)/4 = -1$.

The literature data in Figure 4 is intriguing in that it presents a rather useful demarcation between Zintl pnictides with experimentally-verified n-type dopability (measured electron concentrations) and those for which data on n-type doping is not available. We find that all Zintl compounds with -1 average oxidation state of the pnictide (e.g. As, Sb, Bi) are n-type dopable, while those with average oxidation state less than -1 show proclivity for p-type doping. Therefore, the average oxidation state of the anion, which can be straightforwardly determined from the stoichiometry, seems to be a simple predictor of n-type dopability of Zintl pnictides and as such, could potentially be used as a chemical guide for rapidly identifying n-type dopable Zintls.

Mg_3Sb_2, with -3 average oxidation state of Sb, is the only outlier that has been successfully doped n-type by growing the material under Mg-rich conditions [65]. Considering Mg_3Sb_2 as a Zintl phase, which has been debated [26], the data in Figure 4 indicate that while it may be possible to find n-type dopable Zintl pnictides that disobey the oxidation state guide, the likelihood increases as the average pnictide oxidation state approaches -1.

We know from existing experimental studies that there are a few Zintl pnictides that do not suffer from the p-type doping asymmetry (Figure 4). These include $CoSb_3$, $KGaSb_4$, $KAlSb_4$, and Mg_3Sb_2 that have been doped both p- and n-type [22,25,33,46]. $ZnAs_2$ and $CdAs_2$ are reported only as n-type [39] with lower electron concentrations of $\sim 10^{17}$ cm^{-3}. We observe that the known n-type dopable Zintl pnictides, with the exception of Mg_3Sb_2, all share a simple common feature – the average oxidation state of the pnictide (Pn) in these materials are small negative values (Figure 4). Specifically, the Pn average oxidation state is near -1 in n-type dopable Zintls whereas in most other Zintl phases, the oxidation states range from -2 to -3.

A few preliminary observations that emerge from Figure 4 are: (1) the average Pn oxidation state seems to suggest that the likelihood of finding n-type dopable Zintl pnictides increases for metal-poor chemistries, which offers a simple chemical guide to discover n-type dopable Zintl phases, and (2) the chemical guide needs to be further tested because the empirical data for n-type Zintls is comparitively sparse. Detailed studies have shown that Mg_3Sb_2 is not a layered material and therefore, the Zintl-Klemm concept cannot be used to rationalize its structure. [26] Consequently, Mg_3Sb_2 cannot be considered a Zintl phase. In light of these findings, we have not included Mg_3Sb_2 in Figure 4.

It is not immediately obvious how the Pn average oxidation state is related to the n-type dopability of Zintl pnictides. The high formation energy of "killer" cation vacancies is what makes certain Zintl pnictides n-type dopable. According to Eq. 1, the formation energy of cation vacancies (V_{cation}) depends on the energy difference between the defected and host supercells ($E_{D,q} - E_H$) and the chemical potential of the cation (μ_{cation}). The Fermi energy (E_F) is treated as a free parameter. It is not straightforward to deconvolute the energetic contributions of $E_{D,q} - E_H$ and μ_{cation} to V_{cation} formation energy (Eq. 1) for a wide range of chemistries; however, a plausible explanation for the relation between the average oxidation state and n-type dopability can be gleaned from the stoichiometry of the Zintl phases.

Zintl pnictides with Pn average oxidation state near -1 have uniquely cation-poor chemical compositions; in contrast, p-type Zintl pnictides are cation-rich. For example, in $KGaSb_4$ and $CdAs_2$, the metal-to-pnictide ratio is 0.5 while in $LiZnSb$, $Ca_5Al_2Sb_6$, and $CdSb$ the ratios are 2, 1.2, and 1, respectively. These n-type dopable Zintl pnictides already have cation-poor compositions and formation of cation vacancies would further deplete their cation content, which is likely associated with a stiff energetic cost. As a result, the formation energy of "killer" cation vacancies in cation-poor Zintl pnictides is energetically unfavorable, which creates opportunities for n-type doping of these phases. An analogous example of this effect in non-Zintl chemistries is observed in SnO and SnO_2 – the former has a rela-
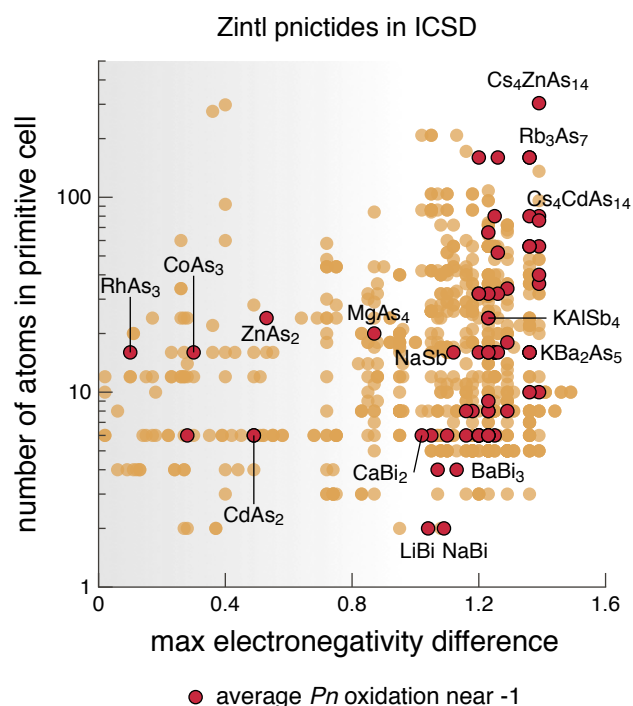
Fig. 5 900 Zintl phases identified from the ICSD denoted by the number of atoms in the primitive cell and the maximum electronegativity difference between the constituent elements. Well-known Zintl phases (*e.g.* ZnSb, $Ca_5Al_2Sb_6$, $CaZn_2Sb_2$, KSnSb) are correctly identified. Red markers denote those Zintl phases where the pnictide average oxidation state is near -1 – based on our proposed chemical guide, these Zintl compounds are predicted to be dopable n-type. Complete list of 900 Zintls phases is documented in the ESI.

tively cation-rich composition compared to the latter. While formation of Sn vacancies (V_{Sn}) in SnO is facile [66,67], the formation of V_{Sn} in SnO_2 is unfavorable [68,69].

Based on the curated experimental data (Figure 4), and first-principles defect calculations presented in Sections 2.2, and 2.3, the proposed chemical guide appears promising for rapid identification of n-type dopable Zintl pnictides. In the next section (Section 2.5), we perform a large-scale search to identify Zintl pnictides that are predicted to exhibit good n-type thermoelectric performance, and expected to be n-type dopable based on their Pn average oxidation state. For three identified candidate materials, we confirm their n-type dopability through first-principles defect calculations, providing further confidence to this approach. To truly demonstrate the usefulness of the approach, we call upon the experimentalists to: (1) synthesize and characterize the promising Zintl pnictides identified in Section 2.5, and (2) perform targeted synthesis of new, undiscovered Zintl phases that satisfy the oxidation state guide. To realize the latter, one may consider chemical substitutions in known Zintl phases with Pn average oxidation state near -1.

2.5 Search for *n*-type Dopable Zintl Pnictides with Promising Thermoelectric Performance

Traditionally, computational searches for novel thermoelectric materials using descriptor-based approaches have either over-looked material dopability alltogether [28,36] or assessed the dopa-bility of the identified candidates *post-search* through first-principles defect calculations or experimental doping stud-ies [25,70]. While dopability can be reliably assessed with first-principles defect calculations, their practical implementation is still computationally expensive such that it cannot be performed for a large set of candidate materials. In this work, the pro-posed chemical guide for identifying *n*-type dopable Zintl pnic-tides presents a unique opportunity to assess material dopability *prior* to gauging their thermoelectric performance – this is en-abled by the simplicity of the chemical guide. With the chem-ical guide, it is possible to rapidly search vast chemical spaces, which would not be possible even with computationally-tractable descriptors of thermoelectric performance such as β [28].

With the goal of accelerating the discovery of *n*-type Zintl thermoelectric materials, we performed a broad search within ~40,000 stoichiometric and ordered structures reported in the In-organic Crystal Structure Database (ICSD) [71] to identify candidate *n*-type dopable Zintl pnictides that are predicted to exhibit good thermoelectric performance. The search was a three-step process involving: (1) automated search of Zintl pnictide structures, (2) identification of Zintl pnictides that are predicted to be dopable *n*-type according to the chemical guide, and (3) assessment of the thermoelectric performance of the *n*-type dopable Zintl pnictides to identify promising candidates.

The methodology for automated search of Zintl pnictide struc-tures is presented in the Methods section. Using the *Pn-Pn* bond as a structural search criteria, we identified 185 binary (78 ar-senides, 73 antimonides, 34 bismuthides), and 160 ternary (50 arsenides, 84 antimonides, 26 bismuthides) compounds. The au-tomated search correctly identifies well-known Zintl compounds such as $ZnSb$, Mo_3Sb_7, $Ca_5Al_2Sb_6$, $Yb_{14}MnSb_{11}$ that have been widely studied as thermoelectric materials. In addition, we ide-tified 555 ternary polar intermetallics, which can be classsified as Zintls. Well-known phases such as $CaZn_2Sb_2$ and $KSnSb$ are correctly identified. The 900 identified Zintl phases are shown in Figure 5, represented by the number of atoms in the primitive cell and the maximum of the electronegativity (Pauling) differences between pairwise combinations of the constituent elements. The maximum electronegativity difference provides a rough measure of the ionicity of the cation-anionic framework bonding.

Among the 900 structures, we identified 67 compounds where the pnictide (As, Sb, Bi) average oxidation state is -1 or higher (red markers in Figure 5) – according to our chemical guide, these Zintl phases are likely *n*-type dopable. For compounds containing cations that assume multiple oxidation states, especially those containing transition metals, the highest oxidation state of the metal was used to determine the average oxidation state of the pnictide. This identification of potentially *n*-type dopable candi-date materials was designed to be conservative. It is notable that these potentially *n*-type dopable Zintl phases cluster on the right

compound	N	$m^*_{\mathrm{DOS,CB}}$	κ_L	μ_n	$\beta_n/\beta_{\mathrm{PbTe}}$
$ZnAs_2$	24	0.04	6.0	2209	1.9
$NaSb$	16	0.42	1.1	36	1.7
$KGaSb_4$	24	0.12	1.0	120	1.5
$NaAs$	16	0.50	1.4	34	1.5
$KAlSb_4$	24	0.14	1.1	103	1.4
$CdAs_2$	6	0.08	6.3	738	1.3
KSb	16	0.60	0.9	15	1.2
Li_3As_7	160	3.72	1.1	2	1.2
Cs_4ZnAs_{14}	304	4.85	0.7	1	1.0
Ba_3As_{14}	34	3.81	1.0	2	0.6
KSb_2	6	0.11	1.0	60	0.6
Cs_3Sb_7	160	4.34	0.5	1	0.6
$CsBi$	32	0.66	0.7	6	0.6
KBi	32	1.10	0.6	3	0.6
$RbSb_2$	6	0.14	0.7	35	0.5
KBa_2As_5	16	0.89	1.2	8	0.5

Table 1 Candidate *n*-type Zintl pnictides predicted to exhibit high thermoelectric performance with relative $\beta_n/\beta_{\mathrm{PbTe}}$ of 0.5 and greater. Properties: number of atoms in the primitive cell (N), conduction band density of states effective mass ($m^*_{\mathrm{DOS,CB}}$) in units of electronic mass m_e, lattice thermal conductivity (κ_L) in W/mK, and intrinsic electron mobility (μ_n) in cm^2/Vs. β_n is expressed relative to the β of *n*-type PbTe.

side of Figure 5 corresponding to larger values of maximum elec-tronegativity difference. From a materials design perspective, the chemical guideline to realize Zintl phases with pnictide average oxidation state of -1 or higher seems to require that the cation be highly electropositive.

Of the 67 Zintl phases, 43 have finite DFT-calculated band gap, for which we computationally assessed their potential for thermo-electric performance using our previously-developed descriptor β (see Refs. 28 and 72 for details). The larger the value of β, the better the predicted thermoelectric performance. The value of β for the assumed *n*-type doped materials, expressed relative to the *n*-type β of PbTe, is presented in Table 1 for the candidate Zintl phases with relative $\beta_n/\beta_{\mathrm{PbTe}}$ of 0.5 and greater. Also, other com-puted properties such as band gap (E_g), conduction band density of states effective mass ($m^*_{\mathrm{DOS,CB}}$), and modeled lattice thermal conductivity (κ_L) and intrinsic electron mobility (μ_n) are tabu-lated. The complete table of β of all 43 Zintl phases can be found in Table S1 in the supplemental information.

In light of the work presented in Ref. 26, it is important to carefully consider if the proposed candidates can be considered as Zintl phases. The goal of this study to provide a simple chem-ical guide that allows rapid screening of thousands of materials to identify promising *n*-type Zintl phases for thermoelectrics. The broad materials search presented here does not forgo the need for in-depth studies of the candidate materials on a case-by-case basis. The proposed Zintl pnictides in Table 1 contain covalent *Pn-Pn* bonds in the anionic framework (see Figures S2 and S3 in the supplementary information). Therefore, the proposed can-didates fulfill one of the basis requirements of the Zintl concept
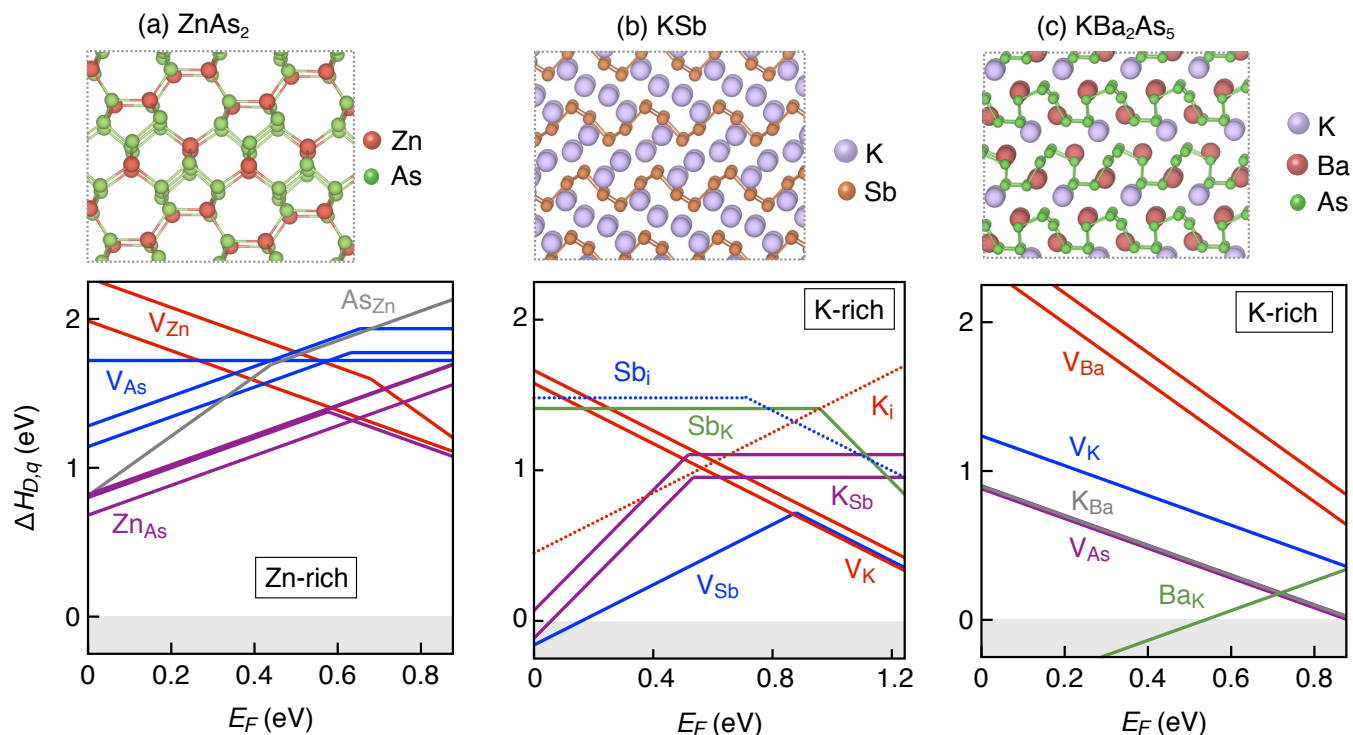
Fig. 6 Formation energies of native defects ($\Delta H_{D,q}$) as functions of Fermi energy (E_F) for (a) ZnAs$_2$, (b) KSb, and (b) KBa$_2$As$_5$ under Zn-rich, K-rich, and K-rich growth conditions, respectively. The corresponding crystal structures are shown above. E_F is referenced to the valence band maximum. The upper limit of E_F shown is the conduction band minimum such that E_F values range from 0 to the band gap. Multiple lines of the same color represent the same defect type at different Wyckoff sites. $\Delta H_{D,q}$ of some defects, particularly interstitials, are outside the energy window shown. The native defect energetics confirm the *n*-type dopability of these candidate materials.

i.e. covalent character of the anionic framework. Additionally, most of the proposed Zintl phases contain highly electropositive cations (Li, Na, K, Ba, Rb, Cs). As a result, the cation-anionic framework bonding will have significant ionic character, thereby fulfilling another requirement of the Zintl concept.

Most notable among the candidate materials are KGaSb$_4$ and KAlSb$_4$ that we have previously demonstrated to be *n*-type dopable Zintls with thermoelectric figure of merit *zT* approaching $\sim$1, without aggressive optimization[24,25]. Specifically, we have demonstrated that Ba-doped KGaSb$_4$ is *n*-type[25] (as well as *p*-type via Zn doping). In addition, first-principles defect calculations of candidate materials KGaSb$_4$ (Figure 3a), CdAs$_2$ (Figure 3b), and KSb (Figure 3c) confirm that these materials are dopable *n*-type. As with other well-known Zintl thermoelectric materials, most Zintl phases in Table 1 exhibit low lattice thermal conductivities. To further confirm the validity of the proposed chemical guide, we performed defect calculations for three candidate materials from Table 1, which are discussed next.

ZnAs$_2$: Based on the value of β_n presented in Table 1, *n*-type ZnAs$_2$ is predicted to exhibit superior thermoelectric performance, mainly arising from its high electron mobility. The formation energetics of the native defects in ZnAs$_2$ grown under Zn-rich conditions, shown in Figure 6(a), suggest that the material is dopable *n*-type. As expected, zinc vacancies are the lowest-energy acceptors but their formation energies are significantly high – larger than 1 eV for Fermi energy at the CBM. Also,

the formation energy of the lowest-energy antisite donors, Zn$_{As}$, are high even under Zn-rich/As-poor growth conditions. The high formation energy of native donor and acceptor defects mean that ZnAs$_2$ is intrinsic when not extrinsically doped. The very high formation energy of the "electron killer" cation vacancies presents the opportunity for extrinsic *n*-type doping of the material.

KSb: The Zintl phase KSb has a LiAs structure type composed of corrugated ...Sb-Sb-Sb... chains interspered with K (Figure 6b). Beside its crystal structure, phase competition with K$_3$Sb, and semiconducting nature, not much is known about KSb regarding its doping behavior. The *Pn* average oxidation state is -1 and according to the proposed chemical guide should be an *n*-type dopable. From the defect energetics shown for K-rich growth conditions (Figure 6b), we find that the cation vacancy (V$_K$) is, as expected, one of the lowest-energy native acceptor defects with a formation energy at the CBM lower than that in KGaSb$_4$ (Figure 3a). However, formation energy of V$_K$ at the CBM is still high enough to not cause significant electron compensation when doped with a suitable extrinsic donor. Additionally, we find that the anion vacancy (V$_{Sb}$) due to its negative-U behavior[73] acts as an amphoteric defect *i.e.* a donor or an acceptor depending on the Fermi energy. The formation energetics are such that the anion vacancy is also one of the lowest-energy acceptor defects (for E_F closer to the conduction band) but its formation energy is about the same as the cation vacancy. Therefore, KSb is an *n*-type dopable Zintl, which further validates the chemical guide.

KBa$_2$As$_5$: Beyond KAlSb$_4$ and KGaSb$_4$, two other ternary Zintl phases feature in Table 1 – Cs$_4$ZnAs$_{14}$ and KBa$_2$As$_5$. Since Cs$_4$ZnAs$_{14}$ has a large unit cell with 304 atoms, first-principles defect calculations is computationally intractable. Therefore, we chose to calculate the formation energetics of native defects in KBa$_2$As$_5$, which are presented in Figure 6(c). The crystal structure of KBa$_2$As$_5$ is characterized by the . . . -As-As-As-. . . backbone with K and Ba in the interstices (Figure 6c). We find that while the defect chemistry of KBa$_2$As$_5$ is unlike other Zintl phases with -1 *Pn* average oxidation state (KGaSb$_4$, CdAs$_2$, ZnAs$_2$, KSb), it is still an *n*-type material, consistent with our predictions. Instead of the expected cation vacancy (V$_K$), the lowest-energy acceptors in KBa$_2$As$_5$ under K-rich conditions are V$_{As}$ vacancies and K$_{Ba}$ antisites. Nevertheless, KBa$_2$As$_5$ is natively self-doped *n*-type with predicted free electron concentrations ranging from $\sim$10^{18} cm^{-3} at 600K to $\sim$10^{19} cm^{-3} at 1000K (Figure S1). The particularly low formation energy of the antisite Ba$_K$ is responsible for the *n*-type self-doping in KBa$_2$As$_5$.

Through these three additional examples (ZnAs$_2$, KSb, KBa$_2$As$_5$), we have further demonstrated that our proposed chemical guide for identifying *n*-type dopable Zintl phases is reliable. Also, the chemical guide is particularly useful to rapidly assess the dopability of Zintl phases with large unit cells, such as Cs$_4$ZnAs$_{14}$, where direct first-principles defect calculations are impractical.

3 Conclusions

In this work, we propose a simple chemical guide for finding novel *n*-type Zintl thermoelectric materials. We find that Zintl pnictides with average oxidation state of the pnictide near -1 are likely *n*-type dopable. Combined with descriptors of thermoelectric performance, the simple chemical guide offers exciting opportunities for synthetic chemists to realize new Zintl pnictides for thermoelectrics with *designed* doping characteristics. More generally, through this work, we demonstrate that it may be possible to describe the dopability of specific material classes with relatively simple compositional and structural descriptors.

Methods

Calculation of Defect Energetics

First-principles defect calculations are performed with density functional theory (DFT) in the generalized gradient approximation of Perdew-Burke-Ernzerhof (PBE)[74], utilizing the projector augmented wave (PAW) formalism as implemented in the VASP software package.[75] Defect energetics are calculated using the standard supercell approach.[29] The total energies of defect supercells are calculated with a plane-wave energy cutoff of 340 eV and a Γ-centered Monkhorst pack k-point grid to sample the Brillouin zone. The defect supercells are relaxed following the procedure used in Refs. 25 and 65. Typically, DFT-calculated total energies (0K) of elemental phases are used as reference elemental chemical potentials (μ_i^0), which can lead to erroneous formation enthalpies.[76] Inspired by the FERE approach[76], the reference chemical potentials in this work are obtained by fitting to a set of measured formation enthalpies.

The underestimation of band gap in DFT-GGA is remedied by

applying band edge shifts as determined from GW quasi-particle energy calculations, following the procedure previously employed in Refs. 25 and 65. The following corrections are included in E_{corr}, following the state-of-the-art methodology described in Ref. 29: (1) image charge correction for charged defects, (2) potential alignment correction for charged defects, (3) band filling correction for shallow defects, and (4) band gap correction for shallow acceptors/donors. The calculation setup and analyses are performed using a software package, pylada-defects, that we have developed to automate point defect calculations.[30]

For a given material, the defect formation energies of all vacancies, antisites, and interstitials are calculated in charge states $q = $ -3, -2, -1, 0, 1, 2, and 3. In most materials considered in this study, the formation energy of interstitials is relatively high; in some cases, interstitial formation energies are larger than the plotted energy window. Vacancies and antisite defects derived from all unique Wyckoff positions in the crystal structure are included in the calculations. The most likely interstitials sites are automatically identified via a Voronoi tessellation scheme as implemented in pylada-defects.[30].

Automated Identification of Zintl Pnictides from ICSD

To search for Zintl pnictides in the Inorganic Crystal Structure Database (ICSD), we developed an algorithmic procedure to automatically identify such structures. Given that all the Zintl pnictides in Figure 4 are arsenides, antimonides, and bismuthides, we limited our search to all structures that contain *Pn* = As, Sb, or Bi, but not N or P. Mixed anion compounds containing *Pn* and one or more of the following anions: O, S, Se, Te, F, Cl, Br, and I, were not considered in this search. The presence of covalent $Pn - Pn$ bonds in the structure is a characteristic feature of many Zintls, including several shown in Figure 4 such as ZnSb, KGaSb$_4$, and Yb$_{14}$MnBi$_{11}$. We identified structures comprising binary, ternary, and quaternary chemistries that contain at least one *Pn-Pn* bond.

Certain polar intermetallic compounds, which lack *Pn-Pn* bonds, can also be classified as Zintl phases because their structures can be rationalized using the Zintl-Klemm concept[77]. Within thermoelectrics, the "1-2-2" (e.g. CaZn$_2$Sb$_2$) and "1-1-1" (e.g. KZnAs) polar intermetallic are considered Zintl phases (Figure 5). We considerd *Pn*-based ternary polar intermetallics with $A_xB_yC_z$ stoichiometry, where A is an electropositive cation, B is a less-electropositive cation that is part of the "anionic framework", and C is a pnictogen (As, Sb, or Bi). The automated search uses the following criteria to identify these structures: (1) at least one bond exists between *B-C*, (2) $\chi_C - \chi_B < 0.7$, and (3) $\chi_C - \chi_A > 1.0$, where χ is the electronegativity on the Pauling scale. This search scheme correctly identifies the well-known "1-1-1" and "1-2-2" phases, as shown in Figure 5. In these Zintl phases, the *Pn* oxidation state is 3-. For the purposes of identifying *n*-type dopable Zintl phases, we are specifically interested in compounds where the *Pn* average oxidation state is -1 or higher, a feature lacking in these Zintl phases.

Conflicts of Interest

There are no conflicts to declare.

Acknowledgements

References

1 S. Kauzlarich, *Chemistry, Structure, and Bonding of Zintl Phases and Ions: Selected Topics and Recent Advances*, Wiley, 1996.

2 I. R. Fisher, S. L. Bud'ko, C. Song, P. C. Canfield, T. C. Ozawa and S. M. Kauzlarich, *Phys. Rev. Lett.*, 2000, **85**, 1120.

3 S.-J. Kim, J. R. Ireland, C. R. Kannewurf and M. G. Kanatzidis, *J. Solid State Chem.*, 2000, **155**, 55.

4 S. Bobev, J. D. Thompson, J. L. Sarrao, M. M. Olmstead, H. Hope and S. M. Kauzlarich, *Inorganic Chemistry*, 2004, **43**, 5044.

5 F. Gascoin, S. Ottensmann, D. Stark, S. M. Haile and G. J. Snyder, *Adv. Funct. Mater.*, 2005, **15**, 1860.

6 S. M. Kauzlarich, S. R. Brown and G. Jeffrey Snyder, *Dalton Trans.*, 2007, **0**, 2099.

7 M. M. Gillett-Kunnath, A. G. Oliver and S. C. Sevov, *J. Amer. Chem. Soc.*, 2011, **133**, 6560.

8 T. Y. Kuromoto, S. M. Kauzlarich and D. J. Webb, *Chem. Mater.*, 1992, **4**, 435.

9 H. Luo, J. W. Krizan, L. Muechler, N. Haldolaarachchige, T. Klimczuk, W. Xie, M. K. Fuccillo, C. Felser and R. J. Cava, *Nature Comm.*, 2015, **6**, 1.

10 R. Marchand and W. Jeitschko, *J. Solid State Chem.*, 1978, **24**, 351.

11 E. S. Toberer, C. A. Cox, S. R. Brown, T. Ikeda, A. F. May, S. M. Kauzlarich and G. J. Snyder, *Adv. Funct. Mater.*, 2008, **18**, 2795.

12 E. S. Toberer, A. Zevalkink, N. Crisosto and G. J. Snyder, *Adv. Funct. Mater.*, 2010, **20**, 4375.

13 A. Zevalkink, W. G. Zeier, G. Pomrehn, E. Schechtel, W. Tremel and G. J. Snyder, *Energy Environ. Sci.*, 2012, **5**, 9121.

14 S. R. Brown, S. M. Kauzlarich, F. Gascoin and G. J. Snyder, *Chem. Mater.*, 2006, **18**, 1873.

15 S. Ohno, U. Aydemir, M. Amsler, J.-H. Pöhls, S. Chanakian, A. Zevalkink, M. A. White, S. K. Bux, C. Wolverton and G. J. Snyder, *Adv. Func. Mater.*, 2017, **27**, 1606361.

16 J. Shuai, Z. Liu, H. S. Kim, Y. Wang, J. Mao, R. He, J. Sui and Z. Ren, *J. Mater. Chem. A*, 2016, **4**, 4312.

17 A. Saramat, G. Svensson, A. E. C. Palmqvist, C. Stiewe, E. Mueller, D. Platzek, S. G. K. Williams, D. M. Rowe, J. D. Bryan and G. D. Stucky, *J. Appl. Phys.*, 2006, **99**, 023708.

18 Y. Hu and S. M. Kauzlarich, *Dalton Trans.*, 2017, **46**, 3996.

19 W. Peng, S. Chanakian and A. Zevalkink, *Inorg. Chem. Front.*, 2018, **5**, 1744.

20 V. Ponnambalam, X. Gao, S. Lindsey, P. Alboni, Z. Su, B. Zhang, F. Drymiotis, M. Daw and T. M. Tritt, *J. Alloys and Compounds*, 2009, **484**, 80.

21 J. Zhang, L. Song, S. H. Pedersen, H. Yin, L. T. Hung and B. B. Iversen, *Nature Comm.*, 2017, **8**, 1–8.

22 H. Tamaki, H. K. Sato and T. Kanno, *Adv. Mater.*, 2016, **28**, 10182.

23 S. Ohno, K. Imasato, S. Anand, H. Tamaki, S. D. Kang, P. Gorai, H. K. Sato, E. S. Toberer, T. Kanno and G. J. Snyder, *Joule*, 2017, **2**, 141.

24 B. R. Ortiz, P. Gorai, L. Krishna, R. Mow, A. Lopez, R. McKinney, V. Stevanovic and E. S. Toberer, *J. Mater. Chem. A*, 2017, **5**, 4036.

25 B. Ortiz, P. Gorai, V. S. Stevanović and E. S. Toberer, *Chem. Mater.*, 2017, **29**, 4523.

26 J. Zhang, L. Song, K. Tolborg and B. B. Iversen, *Nat. Comm.*, 2018, **9**, 4716.

27 J. Zhang, L. Song, G. K. H. Madsen, K. F. F. Fischer, W. Zhang, X. Shi and B. B. Iversen, *Nature Comm.*, 2016, **7**, 1.

28 J. Yan, P. Gorai, B. Ortiz, S. Miller, S. A. Barnett, T. Mason, V. Stevanovic and E. S. Toberer, *Energy Environ. Sci.*, 2015, **8**, 983.

29 S. Lany and A. Zunger, *Phys. Rev. B*, 2008, **78**, 235104.

30 A. Goyal, P. Gorai, H. Peng, S. Lany and V. S. Stevanović, *Comp. Mat. Sci.*, 2016, **130**, 1.

31 A. Goyal, P. Gorai, E. S. Toberer and V. S. Stevanović, *npj Comp. Mater.*, 2017, **3**, 1.

32 G. S. Pomrehn, A. Zevalkink, W. G. Zeier, A. van de Walle and G. J. Snyder, *Angewandte Chemie International Edition*, 2014, **53**, 3422.

33 A. Bhardwaj and D. K. Misra, *RSC Adv.*, 2014, **4**, 34552.

34 L. Bjerg, G. K. H. Madsen and B. B. Iversen, *Chem. Mat.*, 2012, **24**, 2111.

35 E. S. Toberer, A. F. May, C. J. Scanlon and G. J. Snyder, *J. Appl. Phys.*, 2009, **105**, 063701.

36 G. K. H. Madsen, *J. Amer. Chem. Soc.*, 2006, **128**, 12140.

37 S. Wang, Z. Wang, W. Setyawan, N. Mingo and S. Curtarolo, *Phys. Rev. X*, 2011, **1**, 021012.

38 H. Zhu, G. Hautier, U. Aydemir, Z. M. Gibbs, G. Li, S. Bajaj, J.-H. Pohls, D. Broberg, W. Chen, A. Jain, M. A. White, M. Asta, G. J. Snyder, K. Persson and G. Ceder, *J. Mater. Chem. C*, 2015, **3**, 10554.

39 A. Oubraham, G. Biskupski and E. Zdanowicz, *Solid State Comm.*, 1991, **77**, 351.

40 D. Houde, J. Lefaivre, S. Jandl and E. Arushanov, *Solid State Comm.*, 1982, **41**, 325.

41 P. H. M. Böttger, G. S. Pomrehn, G. J. Snyder and T. G. Finstad, *Physica Status Solidi (a)*, 2011, **208**, 2753.

42 Y. Ugai and T. Zyubina, *Neorg. Mater.*, 1966, **2**, 9.

43 E. S. Toberer, P. Rauwel, S. Gariel, J. Tafto and G. Jeffrey Snyder, *J. Mater. Chem.*, 2010, **20**, 9877.

44 J. Wang and K. Kovnir, *J. Amer. Chem. Soc.*, 2015, **137**, 12474.

45 V. Lazarev, V. Shevchenko, I. Grinberg and V. Sobolev, *Moscow Izdatel Nauka*, 1978.

46 T. Caillat, A. Borshchevsky and J.-P. Fleurial, *AIP Conf. Proc.*, 1994, **316**, 58.

47 S. Chanakian, U. Aydemir, A. Zevalkink, Z. M. Gibbs, J.-P. Fleurial, S. Bux and G. Jeffrey Snyder, *J. Mater. Chem. C*, 2015, **3**, 10518.

48 A. Zevalkink, Y. Takagiwa, K. Kitahara, K. Kimura and G. J. Snyder, *Dalton Trans.*, 2014, **43**, 4720.

49 A. Zevalkink, S. Chanakian, U. Aydemir, A. Ormeci, G. Pomrehn, S. Bux, J.-P. Fleurial and G. J. Snyder, *J. Phys.: Condens. Matter*, 2015, **27**, 015801.

50 G. Tan, Y. Zheng and X. Tang, *Appl. Phys. Lett.*, 2013, **103**, 183904.

51 P. F. Qiu, J. Yang, R. H. Liu, X. Shi, X. Y. Huang, G. J. Snyder, W. Zhang and L. D. Chen, *J. Appl. Phys.*, 2011, **109**, 063713.

52 N. Kazem, A. Hurtado, F. Sui, S. Ohno, A. Zevalkink, J. G. Snyder and S. M. Kauzlarich, *Chem. Mater.*, 2015, **27**, 4413.

53 X. Shi, Y. Pei, G. J. Snyder and L. Chen, *Energy Environ. Sci.*, 2011, **4**, 4086.

54 S. R. Brown, S. M. Kauzlarich, F. Gascoin and G. J. Snyder, *J. Solid State Chem.*, 2007, **180**, 1414.

55 V. Ponnambalam, X. Gao, S. Lindsey, P. Alboni, Z. Su, B. Zhang, F. Drymiotis, M. Daw and T. M. Tritt, *J. Alloys and Compounds*, 2009, **484**, 80.

56 A. F. May, E. S. Toberer and G. J. Snyder, *J. Appl. Phys.*, 2009, **106**, 013706.

57 S. I. Johnson, A. Zevalkink and G. J. Snyder, *J. Mater. Chem. A*, 2013, **1**, 4244.

58 A. Zevalkink, E. S. Toberer, W. G. Zeier, E. Flage-Larsen and G. J. Snyder, *Energy Environ. Sci.*, 2011, **4**, 510.

59 U. Aydemir, A. Zevalkink, A. Ormeci, Z. M. Gibbs, S. Bux and G. J. Snyder, *Chem. Mater.*, 2015, **27**, 1622.

60 S. Chanakian, A. Zevalkink, U. Aydemir, Z. M. Gibbs, G. Pomrehn, J.-P. Fleurial, S. Bux and G. J. Snyder, *J. Mater. Chem. A*, 2015, **3**, 10289.

61 Q.-G. Cao, H. Zhang, M.-B. Tang, H.-H. Chen, X.-X. Yang, Y. Grin and J.-T. Zhao, *J. Appl. Phys.*, 2010, **107**, 053714.

62 N. Kazem, J. V. Zaikina, S. Ohno, G. J. Snyder and S. M. Kauzlarich, *Chem. Mater.*, 2015, **27**, 7508.

63 S. K. Bux, A. Zevalkink, O. Janka, D. Uhl, S. Kauzlarich, J. G. Snyder and J.-P. Fleurial, *J. Mater. Chem. A*, 2014, **2**, 215.

64 T. Yi, G. Zhang, N. Tsujii, J.-P. Fleurial, A. Zevalkink, G. J. Snyder, N. Gronbech-Jensen and S. M. Kauzlarich, *Inorg. Chem.*, 2013, **52**, 3787.

65 P. Gorai, B. Ortiz, E. S. Toberer and V. Stevanovic, *J. Mater. Chem. A*, 2018, **6**, 13806.

66 J. P. Allen, D. O. Scanlon, L. F. J. Piper and G. W. Watson, *J. Mater. Chem. C*, 2013, **1**, 8194.

67 J. B. Varley, A. Schleife, A. Janotti and C. G. Van de Walle, *Applied Physics Letters*, 2013, **103**, 082118.

68 D. O. Scanlon and G. W. Watson, *J. Mater. Chem.*, 2012, **22**, 25236.

69 A. Janotti and C. G. Van de Walle, *Physica Status Solidi (b)*, 2011, **248**, 799.

70 A. Faghaninia, G. Yu, U. Aydemir, M. Wood, W. Chen, G.-M. Rignanese, G. J. Snyder, G. Hautier and A. Jain, *Phys. Chem. Chem. Phys.*, 2017, **19**, 6743.

71 A. Belsky, M. Hellenbrandt, V. L. Karen and P. Luksch, *Acta Crystallogr. B*, 2002, **58**, 364.

72 P. Gorai, D. Gao, B. Ortiz, S. Miller, S. Barnett, T. Mason, Q. Lv, V. Stevanovic and E. S. Toberer, *Comp. Mater. Sci.*, 2016, **112A**, 368.

73 G. D. Watkins, *MRS Proc.*, 1980, **2**, 21.

74 J. P. Perdew, K. Burke and M. Ernzerhof, *Phys. Rev. Lett.*, 1996, **77**, 3865.

75 G. Kresse and J. Furthmüller, *Phys. Rev. B*, 1996, **54**, 11169.

76 V. Stevanović, S. Lany, X. Zhang and A. Zunger, *Phys. Rev. B*, 2012, **85**, 115104.

77 H. Schäfer, B. Eisenmann and W. Müller, *Angewandte Chemie*, 1973, **12**, 694.